Science Advances

Gigahertz Modulation of the Full Visible Spectrum via Acoustic Vibrations of Elastically Anisotropic Indium-Tin-Oxide Nanorod Arrays --Manuscript Draft--

Manuscript Number:	ScienceAdvances-D-16-00117
Full Title:	Gigahertz Modulation of the Full Visible Spectrum via Acoustic Vibrations of Elastically Anisotropic Indium-Tin-Oxide Nanorod Arrays
Short Title:	Gigahertz Modulation of the Full Visible Spectrum by Acoustic Vibrations of Elastically Anisotropic Indium-Tin-Oxide Nanorods
Abstract:	Active control of light is important for photonic circuits, optical switching and telecommunications. Coupling light with acoustic vibrations in nanoscale optical resonators offers optical modulation capabilities with high bandwidth and small footprint. Instead of using noble metals, here we introduce indium-tin-oxide nanorod arrays (ITO-NRAs) as the operating media, and demonstrate optical modulations covering the ultraviolet to full-visible spectral range (from 360 nm to 700 nm) with ~ 20 GHz bandwidth through excitation of coherent acoustic vibrations in ITO-NRAs. This broadband modulation results from the collective optical diffraction by the dielectric ITO-NRAs, and a high differential transmission modulation up to 10% is achieved through efficient near-infrared, on-plasmon-resonance pumping. By combining the frequency signatures of the vibrational modes with finite-element simulations, we further determine the anisotropic elastic constants for single-crystalline ITO, which are not known for the bulk phase. This technique to determine elastic constants using coherent acoustic vibrations of uniform nanostructures can be generalized to the study of other inorganic materials.
Article Type:	Research Article
Section/Category:	Physical Sciences
Manuscript Classifications:	Physical sciences; Materials science; Material properties; Physical properties; Anisotropy; Optical properties; Materials; Metamaterials; Optical metamaterials; Nanomaterials; Nanowires; Physics; Acoustics; Acoustic properties; Optics; Condensed matter physics; Light matter interactions; Research methods; Spectroscopy; Laser spectroscopy; Modeling; Computer modeling
Keywords:	ultrafast; nanorod; acoustic vibration; plasmonics; nanophotonics; ultrafast pump- probe spectroscopy; indium-tin-oxide; elasticity; transparent conducting oxides; acoustic phonons
First Author:	Peijun Guo, M.Sc.
Corresponding Author:	Robert P. H. Chang, Ph.D. Northwestern University Evanston, IL UNITED STATES
Corresponding Author E-Mail:	r-chang@northwestern.edu
Corresponding Author's Institution:	Northwestern University
Corresponding Author's Secondary Institution:	
Order of Authors:	Peijun Guo, M.Sc.
	Richard D. Schaller, Ph.D.
	Leonidas E. Ocola, Ph.D.
	John B. Ketterson, Ph.D.
	Robert P. H. Chang, Ph.D.
Order of Authors Secondary Information:	
Corresponding Author Secondary Information:	

Maiken H. Mikkelsen, Ph.D. Suggested Reviewers: Assistant Professor, Duke University m.mikkelsen@duke.edu Prof. Mikkelsen is an expert on ultrafast optics and nanophotonics. Maiken H. Mikkelsen, Ph.D. Assistant Professor, Duke University m.mikkelsen@duke.edu Prof. Mikkelsen is an expert on ultrafast optics and nanophotonics. Gregory V. Hartland, Ph.D. Professor, University of Notre Dame ghartlan@nd.edu Prof. Hartland is an expert and pioneer in ultrafast laser and nanomaterials interactions. Jaime Gómez Rivas, Ph.D. Group leader, FOM-instituut AMOLF J.Gomez@amolf.nl Dr. Rivas is an expert on nanowire plasmonics and nanophotonics. Fabrice Vallée, Ph.D. Professor, Université Lyon 1 fabrice.vallee@univ-lyon1.fr Prof. Vallée is a well-known pioneer in ultrafast laser - matter interactions, and have published a number of seminal papers in this field since the 1990s. Xiang Zhang, Ph.D. Professor, University of California Berkeley xzhang@me.berkeley.edu Prof. Zhang is a leader in the field of plasmonics and nanophotonics. David J. Norris, Ph.D. Professor, ETH Zurich dnorris@ethz.ch Prof. Norris is an expert on optical materials and has more than 20,000 citations. Harry Atwater, Ph.D. Professor, California Institute of Technology haa@caltech.edu Prof. Atwater is a pioneer in plasmonics and nanophotonics, especially those enabled by alternative material platforms such transparent conducting oxides. **Opposed Reviewers:** Otto L. Muskens, Ph.D. Professor, University of Southampton O.Muskens@soton.ac.uk Competing research interests. Alexandra Boltasseva, Ph.D. Associate Professor, Purdue University aeb@purdue.edu Competing research interests. Vladimir Shalaev, Ph.D. Professor, Purdue University shalaev@purdue.edu

Competing research interests.

Robert R. McCormick School of Engineering and Applied Science Northwestern University 2220 Campus Drive Evanston, Illinois 60208-3108 Department of Materials Science and Engineering

Phone 847-491-3537 Fax 847-491-7820



Dear Editor of Science Advances,

Please find the manuscript entitled "Gigahertz Modulation of the Full Visible Spectrum via Acoustic Vibrations of Elastically Anisotropic Indium-Tin-Oxide Nanorod Arrays" by Peijun Guo, Richard D. Schaller, Leonidas E. Ocola, John B. Ketterson and Robert P. H. Chang, which we would like you to consider for publication in *Science Advances* as an *research article*.

Coherent photon-phonon coupling in nanostructures has shown rapid progress due to importance in fundamental sciences (such as optomechanics) and practical applications (such as acousto-optic modulators). Dynamic control of coherent acoustic phonons in nanoscale optical resonators via ultrafast optical excitation offers all-optical transmission modulations with high bandwidth arising from confinement of phonon modes, and spectral tunability that can be achieved by tailoring the nanostructure's geometry. However, the well-explored noble metal plasmonic nanostructures are limited in spectral width (usually around its plasmon resonance; for gold this is usually located in the red to near-infrared range from 650 nm to 900 nm), modulation amplitude (typical differential transmission change is on the order of 0.001% to 1%), and physical robustness (e.g. gold nanostructures can melt at pumping fluences of a few mJ/cm²).

In this work, instead of relying on noble metals, we introduce periodic indium-tin-oxide nanorod arrays (ITO-NRAs) as the operating media. The metallic property of ITO-NRAs in the near-infrared gives rise to a strong localized surface plasmon resonance (LSPR), permitting efficient on-resonance pumping to launch the coherent acoustic vibration modes. The diffractive property of the dielectric ITO-NRAs from 360 nm to 700 nm enables multiple, strong interference-type transmission minima, which is a unique spectral feature that has not been achieved in other established nanorod (or nanowire) systems. By accessing both the metallic and dielectric properties of ITO-NRAs, we demonstrate modulation of a signal beam with ~ 20 GHz frequency, covering an unprecedentedly wide range from the ultraviolet to full visible spectrum (360 nm to 700 nm), with differential transmission modulation up to 10% (10 to 1000 times larger than recent reports such as *Nat. Photonics*, **2009**, 4, 492; *Nat. Comm.*, **2015**, 6, 7002; many other paper only showed in arbitrary units, such as *Nat. Comm.*, **2014**, 5, 4042). We further show that the acoustic vibrations of ITO-NRAs can periodically redistribute intensity between the centered, zeroorder beam and eight oblique, higher-order beams, which can potentially be exploited as active, high-frequency beam-steering optical component.

Equally important, upon comparing the acoustic vibration modes of ITO-NRAs with detailed finite-element simulations, we determine, for the first time, the anisotropic elastic constants of single-crystalline ITO, which is currently one of the most technologically important transparent conducting oxide materials widely used in both research labs and commercial applications. This is the first report that obtains elastic constants from acoustic vibrations using ultrafast spectroscopy for materials where the bulk values are unknown. The technique can potentially be used for determining elastic constants of other inorganic materials when bulk values may be unobtainable (e.g. due to a lack of stability of the bulk phase), provided they can be formed into uniform nanostructures. The elastic properties reported here can also shed light on the fabrication of mechanically robust, existing and emerging ITO-based devices such as electro-optic modulators (*Phys. Rev. Lett.*, **2012**, *109*, 053901; *Nano Lett.*, **2014**, *14*, 6463), in which cases the critical dimensions of ITO are reaching the tens of nanometer scale, comparable to the size of a single grain.

In conclusion, our work not only demonstrates high frequency optical modulation and beam-steering capabilities with particularly broad spectral range and large peak amplitude, but also highlights a new, generalizable, "non-invasive" technique to elucidate the elastic constants for nanostructured, single-crystalline materials. We believe that our work is of broad interest to the nanophotonics, plasmonics, nanoscience, and materials communities, and *Science Advances* is the ideal journal in which to publish this work.

Yours sincerely,

Richard D. Schaller

Scientist, Center for Nanoscale Materials, Argonne National Laboratory Assistant Professor, Department of Chemistry, Northwestern University schaller@anl.gov, schaller@northwestern.edu, 1-630-252-1423

Robert P. H. Chang

Professor, Department of Materials Science and Engineering, Northwestern University r-chang@northwestern.edu, 1-847-491-3598

Gigahertz Modulation of the Full Visible Spectrum via Acoustic Vibrations of Elastically Anisotropic Indium-Tin-Oxide Nanorod Arrays

Peijun Guo¹, Richard D. Schaller^{2, 3, *}, Leonidas E. Ocola², John B. Ketterson⁴, Robert P. H. Chang^{1, *}

¹Department of Materials Science and Engineering, Northwestern University

²Center for Nanoscale Materials, Argonne National Laboratory

³Department of Chemistry, Northwestern University

⁴Department of Physics and Astronomy, Northwestern University

Abstract

Active control of light is important for photonic circuits, optical switching and telecommunications. Coupling light with acoustic vibrations in nanoscale optical resonators offers optical modulation capabilities with high bandwidth and small footprint. Instead of using noble metals, here we introduce indium-tin-oxide nanorod arrays (ITO-NRAs) as the operating media, and demonstrate optical modulations covering the ultraviolet to full-visible spectral range (from 360 nm to 700 nm) with ~ 20 GHz bandwidth through excitation of coherent acoustic vibrations in ITO-NRAs. This broadband modulation results from the collective optical diffraction by the dielectric ITO-NRAs, and a high differential transmission modulation up to 10% is achieved through efficient near-infrared, on-plasmon-resonance pumping. By combining the frequency signatures of the vibrational modes with finite-element simulations, we further determine the anisotropic elastic constants for single-crystalline ITO, which are not known for the bulk phase. This technique to determine elastic constants using coherent acoustic vibrations of uniform nanostructures can be generalized to the study of other inorganic materials.

MAIN TEXT

Introduction

The coupling of light to high frequency acoustic vibrations is of interest for applications such as acousto-optic modulators (1, 2), and also represents an integral part of the emerging field of optomechanics (3-8). The ability to control light with coherent acoustic vibrations in nanoscale optical resonators offers unique opportunities for all-optical modulations with tailored spectral and temporal responses (9). This arises from the strong, shape-dependent confinement that can be achieved for both photons and phonons, which in turn offers enhanced light intensity modulation capabilities with high bandwidths in the gigahertz (GHz) to terahertz (THz) range (10, 11).

Plasmonic noble metal nanostructures have been widely exploited to optically excite and probe phonon modes (12-14). The large absorption cross-sections at localized surface plasmon resonances (LSPRs) facilitate phonon generation by the following mechanism: on-resonance pumping yields a rapid electron temperature rise (in a couple hundred femtoseconds), which is followed by a lattice temperature rise through electron-phonon coupling (in few picoseconds); this impulsive heating and the associated thermal expansion of the lattice have a duration much shorter than vibration periods of nanostructures (nanorods in the present study) and hence excite various high frequency acoustic modes (15, 16). In such experiments, geometrical deformation as well as strain-dependent refractive index changes produce oscillations in the intensity of a transmitted (or reflected) signal beam. However, the usual single resonance and internal loss of plasmonic systems place limits on the achievable wavelength range and modulation strength of the signal beam, with differential transmission modulation on the order of 0.0001% to 1% (17, 18). On the other hand, controllably-doped materials such as transparent conducting oxides that behave as a dielectric in the ultraviolet to visible range offers attractive metallic properties (e.g. LSPRs) in the infrared (19, 20). These materials have robust physical properties such as rigidity and high melting points (21). In particular, indium-tin-oxide (ITO), widely used for solar cells (22), displays (23), light-emitting diodes (24, 25), touch sensors (26), and heat-reflecting glasses (27), has recently been exploited for emerging applications in infrared plasmonics (28, 29), electro-optical modulators (30, 31) and nonlinear optical switching devices (32, 33).

In this work we combine the unique optical and mechanical properties of ITO to achieve strong modulation and steering of light via coherent acoustic vibrations in periodic indium-tinoxide nanorod arrays (ITO-NRAs). Due to the low carrier concentration comparing to noble metals, ITO-NRAs exhibit an LSPR in the near-infrared (NIR), as well as a number of transmission minima in the 360 nm to 700 (defined as UV-vis in the paper) range resulting from collective light diffraction by the periodic array. By resonantly pumping the ITO-NRA, we demonstrate coherent acoustic vibrations which modulate, and steer probe signals in the UV-vis range at ~20 GHz frequency with a maximal differential transmission modulation amplitude up to ~ 10%. In addition, two complementary transient absorption (TA) measurement techniques were employed to probe the UV-vis with delay time windows of 0-1 ns and 0-50 ns; together they permit a detailed investigation of both the breathing and extensional modes of the ITO-NRAs with large aspect-ratio. By comparing the experimental vibration frequencies with finiteelement simulations, we for the first time report the anisotropic elastic tensor for singlecrystalline ITO, which can shed light on the design and integration of mechanically robust, ITObased electronic and optical devices, especially when their critical dimensions approach the tens of nanometer scale (34-38).

Results and Discussion

1. Optical Modulation of the ultraviolet and full-visible spectrum

The ITO-NRA shown in Fig. 1a and 1b was fabricated via a vapor-liquid-solid nanorod growth technique, starting from a periodic array of gold nanoparticle catalysts where the latter were produced by electron beam lithography (28). The array studied has a periodicity of 1 μm, and each nanorod has an average edge length of 180 (±5) nm and height of 2561 (±68) nm, respectively (See Fig. S4 and S5). The ITO-NRA grown epitaxially on a lattice-matched yttria-stabilized zirconia (YSZ) (100) substrate exhibits high size uniformity and alignment over a large area of 0.6 cm by 0.9 cm (See Fig. S9). The strong dip in the transmission spectrum at 1500 nm shown in Fig. 1c arises from the LSPR of the ITO-NRA with electrons oscillating perpendicular to the length of the nanorods (28). Fig. 1d presents the static transmission spectrum of the dielectric ITO-NRA in the UV-vis range from 360 nm to 700 nm at normal incidence. Remarkably, five transmission minima are observed, which arise from destructive

interferences of electromagnetic waves propagating in the nanorod and free space (39). The periodic ITO-NRA acts as a two-dimensional dielectric optical grating; that is illustrated by the schematic drawing (Fig. 2a) and the photograph of a white-light probe diffracted by the ITO-NRA (Fig. 2b). The transmission minima of the forward scattered (0, 0) mode measured at normal incidence (Fig. 1d) are not due to light absorption. Instead, the interference between the diffracted waves that gives rise to transmission maxima at the (1, 0) and (1, 1) grating modes results in transmission minima for the (0, 0) mode.

Having determined the static spectral features, we then studied the ITO-NRA using pump-probe TA experiments. To efficiently excite coherent phonons, we tuned the center wavelength of the pump to the LSPR of the ITO-NRA at 1500 nm. A white light probe in the UV-vis range was used to study the vibration-induced optical modulations. To ensure sampling the array instead of individual nanorod, the pump beam was adjusted to have a diameter of 190 μ m. Both the pump and probe beams were normal to the substrate (as indicated in Fig. 2a).

We first ran TA experiments with delay times ranging from 0 to 1 ns using probe pulses generated via a translational delay stage (see Methods). Fig. 2c shows the measured $\Delta T/T$ spectral map for the (0, 0) mode under a pump fluence of 8.46 mJ/cm². Importantly, at a fixed delay time, the $\Delta T/T$ spectral map exhibits alternating signs, with each zero-crossing-wavelength from a blue, positive $\Delta T/T$ region to its red, adjacent negative $\Delta T/T$ region matching a static transmission minimum (Fig. 1d), manifesting a pump-induced redshift of the entire UV-vis transmission spectrum. From a Drude description of the ITO permittivity,

$$\varepsilon(\omega) = \varepsilon_{\infty}(\omega) - \frac{\omega_p^2}{\omega^2 + i\gamma_p\omega}$$
, the probe lies in the dielectric range of ITO, which is spectrally

isolated from the NIR range that is dominated by the free-electron-like behavior. Pump-induced redshift is expected to originate from a positive change of the background permittivity, $\varepsilon_{\infty}(\omega)$, which in turn produces a stronger dielectric contrast and hence a larger accumulated phase difference between the nanorod and surrounding free space, giving rise to an out-of-phase condition (a transmission minimum) occurring at longer wavelengths than the static case. This intraband pump induced positive change of $\varepsilon_{\infty}(\omega)$ is consistent with ultrafast optical responses of gold nanoparticles, where intraband pump induced Fermi level smearing gives rise to a

modification of interband transitions that further leads to a positive $\varepsilon_{\infty}(\omega)$ change (15, 40, 41) (a detailed study of the $\varepsilon_{\infty}(\omega)$ change of ITO under intraband pumping is outside the scope of the paper).

The coherent acoustic vibrations of the ITO-NRA are manifested by the temporal oscillations of $\Delta T/T$ signal with a period of ~ 50 ps shown in Fig. 2c. Notably, the transmission modulation covers the 360 nm to 700 nm spectral range, with maximal $\Delta T/T$ approaching 0.1 at 564 nm under the highest experimental pump fluence of 24.4 mJ/cm² (See Fig. S8). We note that this broadband modulation is a unique spectral feature that arises from uniform, periodic, large aspect-ratio, dielectric ITO-NRA structure, which permits multiple UV-vis transmission minima due to sufficient phase difference accumulation. In addition, the high-temperature durable, epitaxially anchored ITO-NRA is stable under high pump fluences (beyond 20 mJ/cm²), thereby allowing efficient phonon excitation; this is in sharp contrast to noble metal counterparts that change shape, melt, or peel off from substrates under a few mJ/cm² fluence (42, 43).

Due to the dielectric nature of the ITO-NRA, the vibration-induced modulation of the (0,0) mode intensity should correspond to complementary modulations of the (1,0) and (1,1) modes. This was investigated in our transient absorption measurements by collecting the (1,0) and (1,1) diffracted spots using an optical fiber. Only narrow spectral windows were measured due to the strong spatial dispersion of the higher grating modes (Fig. 2b). The measured $\Delta T/T$ spectral maps for the (1,0) and (1,1) modes, shown in Fig. 2e and 2f, reveal that the vibration-induced $\Delta T/T$ for the (1,0) and (1,1) are opposite in sign to that of the (0,0) mode shown in Fig. 2d, which indicates that instead of being absorptive, the ITO-NRA periodically redistributes intensity between the centered, (0,0) mode and the oblique, higher order modes. This high frequency beam-steering capability, permitting control of both intensity and direction, is a unique feature of ITO-NRA that cannot be easily achieved by metallic nanostructures due to weaker diffraction arising from their optical loss in similar spectral ranges.

2. Studying elastic properties of ITO

The frequency signatures of the $\Delta T/T$ spectral map for the (0, 0) mode (Fig. 2c), which appear in the Fourier transform shown in Fig. 3a, exhibit two prominent features centered around

20 GHz. From Fig. 3a we find that the negative $\Delta T/T$ maxima centered around 507 nm and 613 nm primarily oscillate a single frequency, whereas all other positive and negative $\Delta T/T$ maxima, such as that at 475 nm, contain two frequencies. This is further supported by Fig. 3b, which shows the time evolution of $\Delta T/T$ and their Fourier transform at 475 nm and 507 nm. We find the 475-nm response involves a peak at 18.5 GHz with a full-width-half-maximum (FWHM) of 1.23 GHz, and a second peak at 22.1 GHz with a FWHM of 1.21 GHz. In contrast, the 507-nm response exhibits a single peak of 18.9 GHz with a FWHM of 1.49 GHz. As indicated in Fig. 3b, the beating of the two vibration modes at 475 nm leads to a cancellation of the vibration-induced ΔT/T signal. Since the frequency difference of 0.4 GHz between 18.5 GHz and 18.9 GHz is significantly smaller than the FWHMs of each peak, we assign these two frequencies to the same mode, and take their average of 18.7 GHz as the frequency of this mode; the 0.4 GHz difference likely arises from slight tapering of the ITO nanorod, and different spatial coupling of the electric and displacement fields at these two wavelengths. The time dependence and associated Fourier transform for the (1, 0) and (1, 1) modes at 475 nm and 507 nm are shown in Fig. 3c and 3d. respectively. We note that the (1, 0) mode exhibits two frequencies at 475 nm with equal weights, but only one frequency of 18.9 GHz at 507 nm. For the (1, 1) mode, however, a single frequency is observed at both wavelengths. Hence the 22.1 GHz oscillation appearing in the (0, 0) mode is only related to the (1, 0) mode, whereas the 18.7 GHz oscillation in the (0, 0) mode is correlated with both the (1, 0) and (1, 1) modes.

Nanorods exhibit three dominant vibration modes, namely breathing, extensional and bending modes; the first two correspond to expansion and compression along the radial and longitudinal directions, respectively (44-47). The frequencies of the breathing and extensional modes are inversely proportional to the radial and longitudinal dimensions (46), and are expected to differ by an order of magnitude in our nanorods (aspect ratio here is 14). Since ~ 100-nm radius nanorods exhibit breathing modes at a few to tens of GHz (45, 48, 49), we assign the 18.7 GHz and 22.1 GHz frequencies to the *1st* and *2nd breathing modes* of the ITO-NRA, respectively. These two modes are consistent with observations in pentagonal gold nanowires (48), in which the displacement fields for the two modes concentrate in corners and edges, respectively, a result of the symmetry breaking for non-cylindrical cross-sections.

To determine the elastic properties of ITO based on the vibration frequencies, we performed finite-element simulations using COMSOL Multiphysics. Since computations for a long aspect-ratio nanorod with sharp corners are computationally expensive, we first reduced the problem to a two-dimensional (2D) cross-section; this accurately captures the vibrational behaviors of the breathing modes which are dominated by displacements within the cross-sectional plane.

Justifications regarding use of the 2D model appears in the SI section 1 and Fig. S1. Full three-dimensional (3D) simulations for a unit cell of the periodic ITO-NRA were also performed and agree well with 2D simulation results. In all simulations the theoretical density of 7.16 g/cm³ for ITO was assumed (See SI section 7).

We first attempted simulations by taking ITO to be an isotropic material described by the Young's modulus, E, and Poisson's ratio, v (see SI section 2). As shown in Fig. S2 and S3, for all possible E and v values, the simulations cannot produce the two observed breathing modes with frequencies of 18.7 and 22.1 GHz. This strongly suggests that the isotropic elastic model of ITO cannot capture the vibrational behaviors of our single-crystalline ITO-NRA, and hence it is expected to be intrinsically anisotropic. To clarify the effects of anisotropy we performed 2D simulations using the three elastic constants, C₁₁, C₁₂ and C₄₄, those are required to characterize the cubic ITO. We varied these constants over a wide range until the two simulated breathing mode frequencies agreed with experimental values. Fig. 4a, 4b and 4c show the plots of the frequency-dependent integration of volumetric strain over the square cross-section for varying values of C_{11} , C_{12} and C_{44} . We find that C_{11} shifts the frequencies of both modes, C_{12} has little effect on the frequencies but tunes the relative strength of the two modes, and C₄₄ mainly affects the frequency of the 2nd mode as well as the relative strength of the two modes. Note that in each panel only one elastic constant was swept. The fixed values in the sweeps for C₁₁, C₁₂ and C₄₄ are 277.5 GPa, 107 GPa and 33.8 GPa, respectively, which, as shown below, are our best estimates of the elastic constants for ITO. Fig. 4d shows the displacement fields for the two breathing modes, which are maximized at the corners and faces for the respective 1st and 2nd breathing modes (See Fig. S6 and S7). Whereas experiment and modeling combine to indicate elastic constant values for C₁₁ of 277.5 GPa and C₄₄ of 33.8 GPa, C₁₂ only adjusts the relative strength of the two modes and hence cannot be uniquely determined as relayed in Fig. 4c: the measured $\Delta T/T$ oscillations result from a poorly understood strain dependent permittivity, hence

correlating the relative strengths of the two modes from simulations with the optical signals was not attempted.

In order to determine C_{12} , we further examined the extensional mode of the ITO-NRA using a different TA experiment, in which a maximal delay time of ~ 50 ns was realized via electronically delayed white light probe pulses (See Methods). The measured $\Delta T/T$ spectral map and associated Fourier transform are shown in Fig. 5a and 5b, from which we find an oscillation frequency with a weighted average of 0.524 GHz and a standard deviation of 0.141 GHz. To understand the extensional mode we performed 3D simulation for a unit cell composed of a single ITO nanorod anchored on YSZ substrate. As there is no adhesion layer between ITO and YSZ (the growth is epitaxial), no thin elastic layer was used in our 3D simulation. This is in contrast to the gold/titanium/glass structures reported elsewhere, in which the titanium alters the vibrational frequencies of the gold particles (9, 12). We treat the single-crystalline, cubic symmetry YSZ substrate using the reported elastic constants $C_{11} = 403.5$ GPa, $C_{12} = 102.4$ GPa and $C_{44} = 59.9$ GPa (50) and a density of 6.0 g/cm³, respectively (51). Keeping $C_{11} = 277.5$ GPa and $C_{44} = 33.8$ GPa for ITO (determined from the breathing mode frequencies), we varied C_{12} from 40 GPa to 130 GPa in the 3D simulations. Fig. 5c shows the displacements of the tip center along the nanorod long axis as a function of vibration frequency for different C₁₂ values. Note that the extensional mode of the ITO-NRA is manifested as a peak in the tip displacement versus frequency curves, so Fig. 5c suggests that increasing C₁₂ yields a lower extensional mode frequency. A C₁₂ of 107 GPa provided the closest match between the experiments and simulations. Using the three determined elastic constants, we performed full 3D simulations for the extensional and breathing modes. Fig. 5d shows the color-coded displacement amplitude along the nanorod long axis for the extensional mode, which monotonically increases from the bottom to the top of the nanorod. Fig. 5d also shows the color-coded amplitude of the total displacement for the 3D simulations of the two breathing modes, which match well with the 2D cross-section analogue shown in Fig. 4d from 2D simulations.

With the three elastic constants in hand, we determine Young's modulus of ITO along any crystalline direction (See SI section 3). The Young's modulus of ITO along its three primary directions are determined to be $E_{[1\ 0\ 0]} = 217.9$ GPa, $E_{[1\ 1\ 0]} = 110.5$ GPa and $E_{[1\ 1\ 1]} = 94.9$ GPa, which suggests that ITO is elastically anisotropic, as further presented graphically by the

orientation dependent Young's modulus diagram in Fig. 6a. The Young's modulus for crystal directions lying in the three low-index (100), (110) and (111) planes are plotted in Fig. 6b, 6c and 6d, respectively. Based on the single-crystalline elasticity, we further estimate the lower and upper bounds on the Young's modulus for polycrystalline ITO, and compare with literature reported values (See SI section 4).

Conclusion

In conclusion, we have demonstrated robust GHz optical modulation and beam-steering capabilities covering the ultraviolet to full-visible spectrum enabled by coherent acoustic vibrations of periodic, uniform ITO-NRAs. Such high-frequency, broadband modulation have not been previously demonstrated and the peak amplitude changes in transmission are particularly large, which opens the door to active, compact, wide-bandwidth optical components. Second, by comparing the experimental vibration frequencies with simulations, we determined the anisotropic elastic constants of single-crystalline ITO in the absence of information on the bulk values. The scheme demonstrated here can potentially facilitate determination of the elastic constants of other crystalline materials where the bulk values are unknown owing to lack of the large single crystals needed for ultrasonic measurements (52) or the difficulty of growing smooth single-crystalline films along multiple orientations as required for nano-indentation measurements (as minimization of surface energy favors film termination in the most stable surfaces (53-55) regardless of the film growth direction), provided they can be formed into uniform nanostructured arrays.

Materials and Methods

Sample fabrication.

The procedure was based on a previous report (28) but slightly modified. Briefly, a 10 nm epitaxial ITO film was sputtered on a YSZ (001) substrate at 600 °C at 5 mTorr under Ar. After spin-coating 70 nm GL-2000 electron beam resist (Gluon Labs), an array of 150 nm dots with designed pitch sizes was exposed on the substrate using JEOL 9300 electron beam lithography system. The sample was then developed in Xylene at room temperature for 1 min and rinsed with IPA. Depositing 2 nm Cr and 15 nm Au followed by lift-off in Anisole at 75 °C for 1 hour then generates the catalyst array. The nanorod growth was performed in a customized tube furnace system. The source (100 mg In and SnO mixture with molar ratio of 9:1) and substrate temperatures were 900°C and 840 °C, respectively. The gas was a mixture of 5% O₂ (balanced by N₂) at 6 sccm and pure Ar at 80 sccm under a total pressure of 130 mTorr.

Static Optical measurements.

The near-infrared transmission spectrum was measured with FTIR (Thermo Nicolet 6700). A ZnSe lens was used to focus the light into a 1 mm diameter spot. The UV-vis transmission spectrum was measured with an UV/Vis/NIR spectrophotometer (Perkin Elmer Lambda 1050).

Transient absorption measurement.

Transient absorption measurements with delay time up to 1 ns were performed using a 35 fs amplified titanium:sapphire laser operating at 800 nm with a repetition rate of 2 kHz. Broadband probe pulses were generated by focusing a portion of the amplifier output into a 2 mm thick CaF_2 window. Pump pulses at 1500 nm were generated via a white light seeded optical parametric amplifier and were reduced in repetition rate to 1 kHz. Probe pulses were time delayed using a mechanical translation stage and retroreflector. The pump spot diameter on the sample was 190 μ m.

Longer pump-probe time delay (0 to 50 ns) transient absorption measurements were performed with ~ 100 ps time resolution using a 100 fs pump pulse and an electronically delayed white light probe pulse. The probe pulse is generated via self-phase modulation of a Nd:YAG

laser in a photonic crystal fiber. Instabilities in the probe pulse were compensated by monitoring a beam-split portion of the pulse in a separate detector. Signal to noise ratios achieved with this system are notably lower than that obtained with the higher time-resolution transient absorption system primarily owing to lower pulse-to-pulse stability of the probe. The pump spot diameter on the sample for the latter measurements was $220 \, \mu m$.

The differential transmission change, $\Delta T/T$, is defined as $[T(t)-T_0)]/T_0$, with T_0 and T(t) denoting the static transmission and transmission at delay time t, respectively.

Finite-element simulations.

Acoustic simulations were performed with the Structural Mechanics module of COMSOL Multiphysics in the frequency domain. A uniform strain in the entire simulation domain was applied and the vibrational response of the nanorod was subsequently analyzed. More simulation details can be found in the SI.

Supplementary Materials

Additional information can be found in a separate Supplementary Materials document.

Corresponding Authors

Richard D. Schaller (schaller@anl.gov, schaller@northwestern.edu)

Robert P. H. Chang (r-chang@northwestern.edu)

References and Notes

- 1. S. Kapfinger *et al.*, Dynamic acousto-optic control of a strongly coupled photonic molecule. *Nat Commun* **6**, (2015).
- 2. B. E. A. Saleh, M. C. Teich, in *Fundamentals of Photonics*. (John Wiley & Sons, Inc., 2001), pp. 799-831.
- 3. E. Gil Santos *et al.*, High-frequency nano-optomechanical disk resonators in liquids. *Nat Nano* **10**, 810-816 (2015).
- 4. L. Ding *et al.*, High Frequency GaAs Nano-Optomechanical Disk Resonator. *Physical Review Letters* **105**, 263903 (2010).

- 5. G. Bahl *et al.*, Brillouin cavity optomechanics with microfluidic devices. *Nat Commun* **4**, (2013).
- 6. A. H. Safavi-Naeini *et al.*, Electromagnetically induced transparency and slow light with optomechanics. *Nature* **472**, 69-73 (2011).
- 7. I. Favero, K. Karrai, Optomechanics of deformable optical cavities. *Nat Photon* **3**, 201-205 (2009).
- 8. N. I. Zheludev, E. Plum, Reconfigurable nanomechanical photonic metamaterials. *Nat Nano* **11**, 16-22 (2016).
- 9. W.-S. Chang *et al.*, Tuning the acoustic frequency of a gold nanodisk through its adhesion layer. *Nat Commun* **6**, (2015).
- 10. S. A. Tadesse, M. Li, Sub-optical wavelength acoustic wave modulation of integrated photonic resonators at microwave frequencies. *Nat Commun* **5**, (2014).
- 11. R. Van Laer, B. Kuyken, D. Van Thourhout, R. Baets, Interaction between light and highly confined hypersound in a silicon photonic nanowire. *Nat Photon* **9**, 199-203 (2015).
- 12. K. O'Brien *et al.*, Ultrafast acousto-plasmonic control and sensing in complex nanostructures. *Nat Commun* **5**, (2014).
- 13. M. Pelton *et al.*, Damping of acoustic vibrations in gold nanoparticles. *Nat Nano* **4**, 492-495 (2009).
- 14. V. Juvé *et al.*, Probing Elasticity at the Nanoscale: Terahertz Acoustic Vibration of Small Metal Nanoparticles. *Nano Letters* **10**, 1853-1858 (2010).
- 15. G. V. Hartland, Optical Studies of Dynamics in Noble Metal Nanostructures. *Chemical Reviews* **111**, 3858-3887 (2011).
- 16. M. Perner *et al.*, Observation of Hot-Electron Pressure in the Vibration Dynamics of Metal Nanoparticles. *Physical Review Letters* **85**, 792-795 (2000).
- 17. T. Schumacher *et al.*, Nanoantenna-enhanced ultrafast nonlinear spectroscopy of a single gold nanoparticle. *Nat Commun* **2**, 333 (2011).
- 18. T. A. Kelf *et al.*, Ultrafast Vibrations of Gold Nanorings. *Nano Letters* **11**, 3893-3898 (2011).
- 19. A. Boltasseva, H. A. Atwater, Low-Loss Plasmonic Metamaterials. *Science* **331**, 290-291 (2011).

- 20. E. Sachet *et al.*, Dysprosium-doped cadmium oxide as a gateway material for mid-infrared plasmonics. *Nat Mater* **14**, 414-420 (2015).
- 21. U. Guler, A. Boltasseva, V. M. Shalaev, Refractory Plasmonics. *Science* **344**, 263-264 (2014).
- J. Zhu, C.-M. Hsu, Z. Yu, S. Fan, Y. Cui, Nanodome Solar Cells with Efficient Light Management and Self-Cleaning. *Nano Letters* 10, 1979-1984 (2010).
- 23. U. Betz, M. Kharrazi Olsson, J. Marthy, M. F. Escolá, F. Atamny, Thin films engineering of indium tin oxide: Large area flat panel displays application. *Surface and Coatings Technology* **200**, 5751-5759 (2006).
- 24. M. G. Helander *et al.*, Chlorinated Indium Tin Oxide Electrodes with High Work Function for Organic Device Compatibility. *Science* **332**, 944-947 (2011).
- 25. H. Kim *et al.*, Indium tin oxide thin films for organic light-emitting devices. *Applied Physics Letters* **74**, 3444-3446 (1999).
- 26. V. Maheshwari, R. F. Saraf, High-Resolution Thin-Film Device to Sense Texture by Touch. *Science* **312**, 1501-1504 (2006).
- 27. A. Hjortsberg, I. Hamberg, C. G. Granqvist, Transparent and heat-reflecting indium tin oxide films prepared by reactive electron beam evaporation. *Thin Solid Films* **90**, 323-326 (1982).
- 28. S. Q. Li *et al.*, Infrared Plasmonics with Indium–Tin-Oxide Nanorod Arrays. *ACS Nano* 5, 9161-9170 (2011).
- 29. G. Garcia *et al.*, Dynamically Modulating the Surface Plasmon Resonance of Doped Semiconductor Nanocrystals. *Nano Letters* **11**, 4415-4420 (2011).
- 30. H. W. Lee *et al.*, Nanoscale Conducting Oxide PlasMOStor. *Nano Letters* **14**, 6463-6468 (2014).
- A. V. Krasavin, A. V. Zayats, Photonic Signal Processing on Electronic Scales: Electro-Optical Field-Effect Nanoplasmonic Modulator. *Physical Review Letters* 109, 053901 (2012).
- 32. M. Abb, Y. Wang, C. H. de Groot, O. L. Muskens, Hotspot-mediated ultrafast nonlinear control of multifrequency plasmonic nanoantennas. *Nat Commun* **5**, (2014).
- 33. D. B. Tice *et al.*, Ultrafast Modulation of the Plasma Frequency of Vertically Aligned Indium Tin Oxide Rods. *Nano Letters* **14**, 1120-1126 (2014).

- 34. S. C. Riha, M. J. DeVries Vermeer, M. J. Pellin, J. T. Hupp, A. B. F. Martinson, Hematite-based Photo-oxidation of Water Using Transparent Distributed Current Collectors. *ACS Applied Materials & Interfaces* **5**, 360-367 (2013).
- 35. B. Lee, P. Guo, S.-Q. Li, D. B. Buchholz, R. P. H. Chang, Three Dimensional Indium—Tin-Oxide Nanorod Array for Charge Collection in Dye-Sensitized Solar Cells. *ACS Applied Materials & Interfaces* **6**, 17713-17722 (2014).
- 36. S. A. Gregory, Y. Wang, C. H. de Groot, O. L. Muskens, Extreme Subwavelength Metal Oxide Direct and Complementary Metamaterials. *ACS Photonics* **2**, 606-614 (2015).
- 37. M. Abb, P. Albella, J. Aizpurua, O. L. Muskens, All-Optical Control of a Single Plasmonic Nanoantenna–ITO Hybrid. *Nano Letters* **11**, 2457-2463 (2011).
- 38. J. Yoon *et al.*, Ultrathin silicon solar microcells for semitransparent, mechanically flexible and microconcentrator module designs. *Nat Mater* **7**, 907-915 (2008).
- 39. S.-Q. Li, K. Sakoda, J. B. Ketterson, R. P. H. Chang, Broadband resonances in indiumtin-oxide nanorod arrays. *Applied Physics Letters* **107**, 031104 (2015).
- 40. N. Del Fatti, F. Vallée, C. Flytzanis, Y. Hamanaka, A. Nakamura, Electron dynamics and surface plasmon resonance nonlinearities in metal nanoparticles. *Chemical Physics* **251**, 215-226 (2000).
- 41. C. Voisin *et al.*, Ultrafast electron-electron scattering and energy exchanges in noblemetal nanoparticles. *Physical Review B* **69**, 195416 (2004).
- 42. M. Gordel *et al.*, Post-synthesis reshaping of gold nanorods using a femtosecond laser. *Physical Chemistry Chemical Physics* **16**, 71-78 (2014).
- 43. W. Li *et al.*, Refractory Plasmonics with Titanium Nitride: Broadband Metamaterial Absorber. *Advanced Materials* **26**, 7959-7965 (2014).
- 44. P. V. Ruijgrok, P. Zijlstra, A. L. Tchebotareva, M. Orrit, Damping of Acoustic Vibrations of Single Gold Nanoparticles Optically Trapped in Water. *Nano Letters* **12**, 1063-1069 (2012).
- 45. S. O. Mariager *et al.*, Direct Observation of Acoustic Oscillations in InAs Nanowires. *Nano Letters* **10**, 2461-2465 (2010).
- 46. M. Hu et al., Vibrational Response of Nanorods to Ultrafast Laser Induced Heating: Theoretical and Experimental Analysis. Journal of the American Chemical Society 125, 14925-14933 (2003).

- 47. P.-A. Mante, C.-Y. Ho, L.-W. Tu, C.-K. Sun, Interferometric detection of extensional modes of GaN nanorods array. *Opt. Express* **20**, 18717-18722 (2012).
- 48. K. Yu *et al.*, Compressible Viscoelastic Liquid Effects Generated by the Breathing Modes of Isolated Metal Nanowires. *Nano Letters*, (2015).
- 49. Y. Li *et al.*, Ultrafast Electron and Phonon Response of Oriented and Diameter-Controlled Germanium Nanowire Arrays. *Nano Letters* **14**, 3427-3431 (2014).
- 50. H. M. Kandil, J. D. Greiner, J. F. Smith, Single-Crystal Elastic Constants of Yttria-Stabilized Zirconia in the Range 20° to 700°C. *Journal of the American Ceramic Society* **67**, 341-346 (1984).
- 51. K. W. Schlichting, N. P. Padture, P. G. Klemens, Thermal conductivity of dense and porous yttria-stabilized zirconia. *Journal of Materials Science* **36**, 3003-3010 (2001).
- 52. W. P. Mason, Physical Acoustics and the Properties of Solids. *The Journal of the Acoustical Society of America* **28**, 1197-1206 (1956).
- 53. K. H. L. Zhang, A. Walsh, C. R. A. Catlow, V. K. Lazarov, R. G. Egdell, Surface Energies Control the Self-Organization of Oriented In2O3 Nanostructures on Cubic Zirconia. *Nano Letters* **10**, 3740-3746 (2010).
- 54. S. A. Chambers, Epitaxial growth and properties of thin film oxides. *Surface Science Reports* **39**, 105-180 (2000).
- 55. T. Naoaki, M. Mikako, K. Masayuki, Y. Itaru, S. Yuzo, Effect of Sn Doping on the Crystal Growth of Indium Oxide Films. *Japanese Journal of Applied Physics* **37**, 6585 (1998).
- 56. R. P. Ingel, D. L. Iii, Elastic Anisotropy in Zirconia Single Crystals. *Journal of the American Ceramic Society* **71**, 265-271 (1988).
- 57. R. Hill, The Elastic Behaviour of a Crystalline Aggregate. *Proceedings of the Physical Society. Section A* **65**, 349 (1952).
- 58. D. G. Neerinck, T. J. Vink, Depth profiling of thin ITO films by grazing incidence X-ray diffraction. *Thin Solid Films* **278**, 12-17 (1996).
- 59. L. Byung-Kee, S. Yong-Ha, Y. Jun-Bo, in *Micro Electro Mechanical Systems*, 2009. *MEMS 2009. IEEE 22nd International Conference on.* (2009), pp. 148-151.
- 60. K. Zeng *et al.*, Investigation of mechanical properties of transparent conducting oxide thin films. *Thin Solid Films* **443**, 60-65 (2003).

- N. Nadaud, N. Lequeux, M. Nanot, J. Jové, T. Roisnel, Structural Studies of Tin-Doped Indium Oxide (ITO) and In4Sn3O12. *Journal of Solid State Chemistry* 135, 140-148 (1998).
- 62. D. Hohnholz, K.-H. Schweikart, M. Hanack, A Simple Method for the Subdivision of ITO Glass Substrates. *Advanced Materials* **11**, 646-649 (1999).

Acknowledgements and Funding: The work was funded by the MRSEC program (NSF DMR-1121262) at Northwestern University. Use of the Center for Nanoscale Materials was supported by the U. S. Department of Energy, Office of Science, Office of Basic Energy Sciences, under Contract No. DE-AC02-06CH11357. The work made use of the EPIC facility (NUANCE Center-Northwestern University), which has received support from the MRSEC program (NSF DMR-1121262) at the Materials Research Center, the International Institute for Nanotechnology (IIN) and the State of Illinois through the IIN. The work also utilized the Northwestern University Micro/Nano Fabrication Facility (NUFAB), which is supported by the State of Illinois and Northwestern University. Author Contributions: P.G., R.D.S. and R.P.H.C. designed the research. P.G. fabricated the sample, performed static measurements and simulations, and analyzed data; R.D.S. performed TA experiments; L.E.O. assisted electron beam fabrication; J.B.K. contributed to the analysis of the vibrational modes. All authors discussed the results. P.G. prepared the manuscript with input and editing from all authors. R.P.H.C. supervised the project. Competing Interests: The authors declare no competing financial interests.

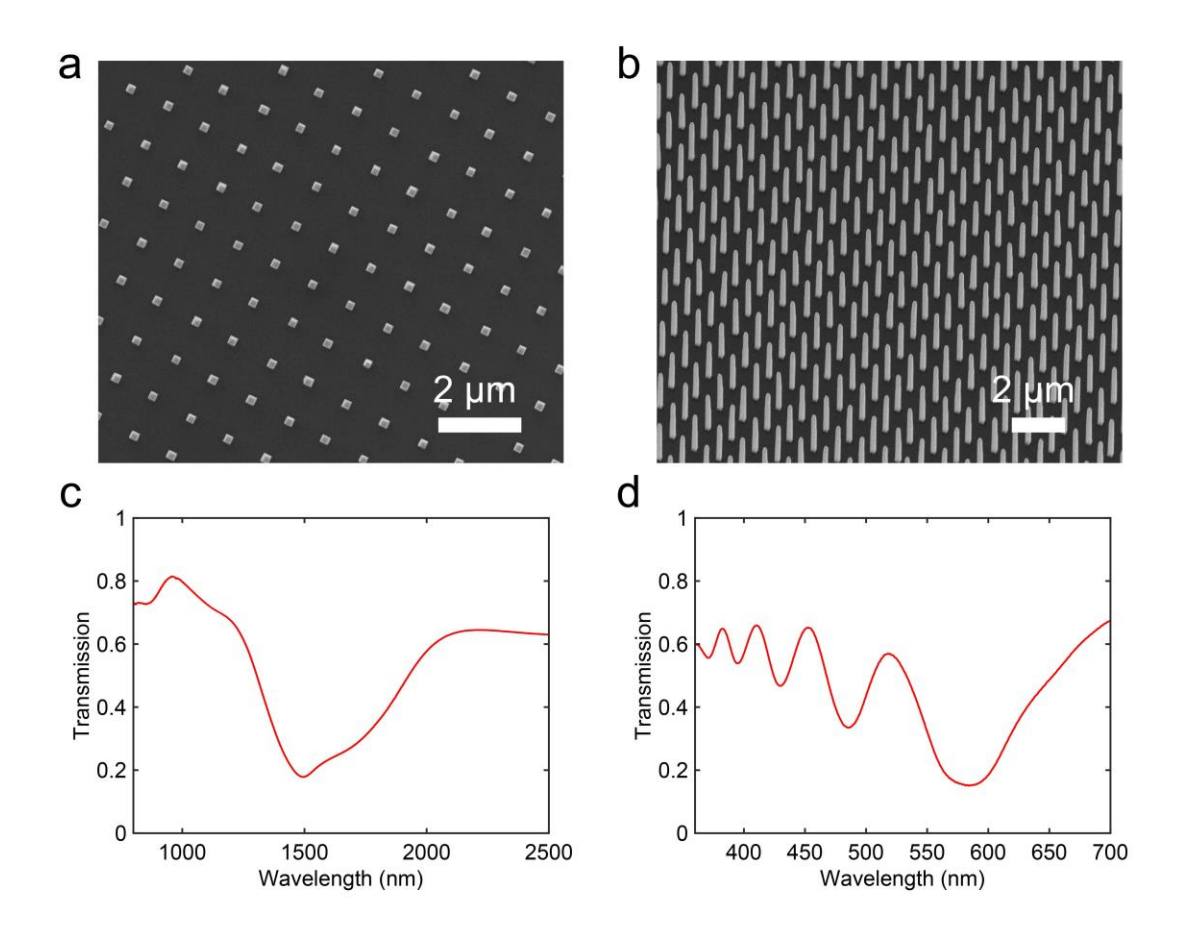


Fig. 1. SEM and static optical characterizations of the ITO-NRA. a, **b** Top-down and 30° views of the ITO-NRA under scanning electron microscope. **c**, Transmission spectra of the ITO-NRA in the NIR range (800 nm to 2500 nm) at normal incidence (referenced to air). **d**, Transmission spectra of the ITO-NRA in the UV-visible range (360 nm to 700 nm) at normal incidence (referenced to air).

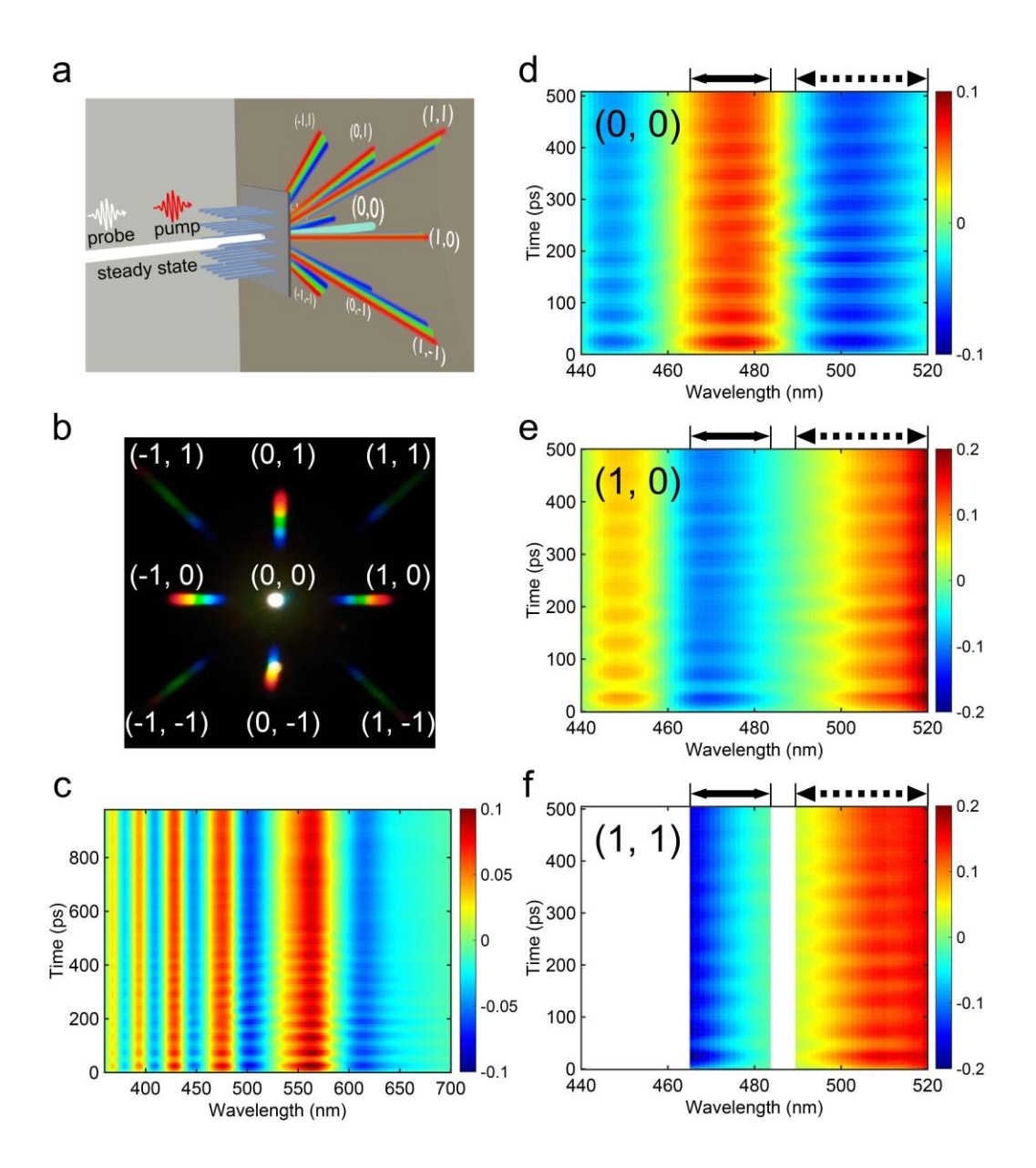


Fig. 2. Transient absorption measurements of the ITO-NRA. **a**, Schematic diagram of the static and transient absorption measurements (the transmitted higher order grating modes are represented by the red-green-blue rays). **b**, Photograph of the diffraction spots produced from a white-light probe transmitted through the sample at normal incidence. **c**, $\Delta T/T$ spectral map of the (0,0) mode for spectral range between 360 nm to 700 nm with delay time up to 1 ns. Pump fluence is 8.46 mJ/cm². **d**, **e**, **f**, $\Delta T/T$ spectral maps of the (0,0), (1,0) and (1,1) modes, respectively, plotted for delay times up to 500 ps. The solid arrow indicates the spectral window from 465 nm to 480 nm, and the dotted arrow indicates the spectral window from 490 nm to 520 nm. Data for the (0,0) mode is same as in **c**, but truncated in **d** for ease of comparison.

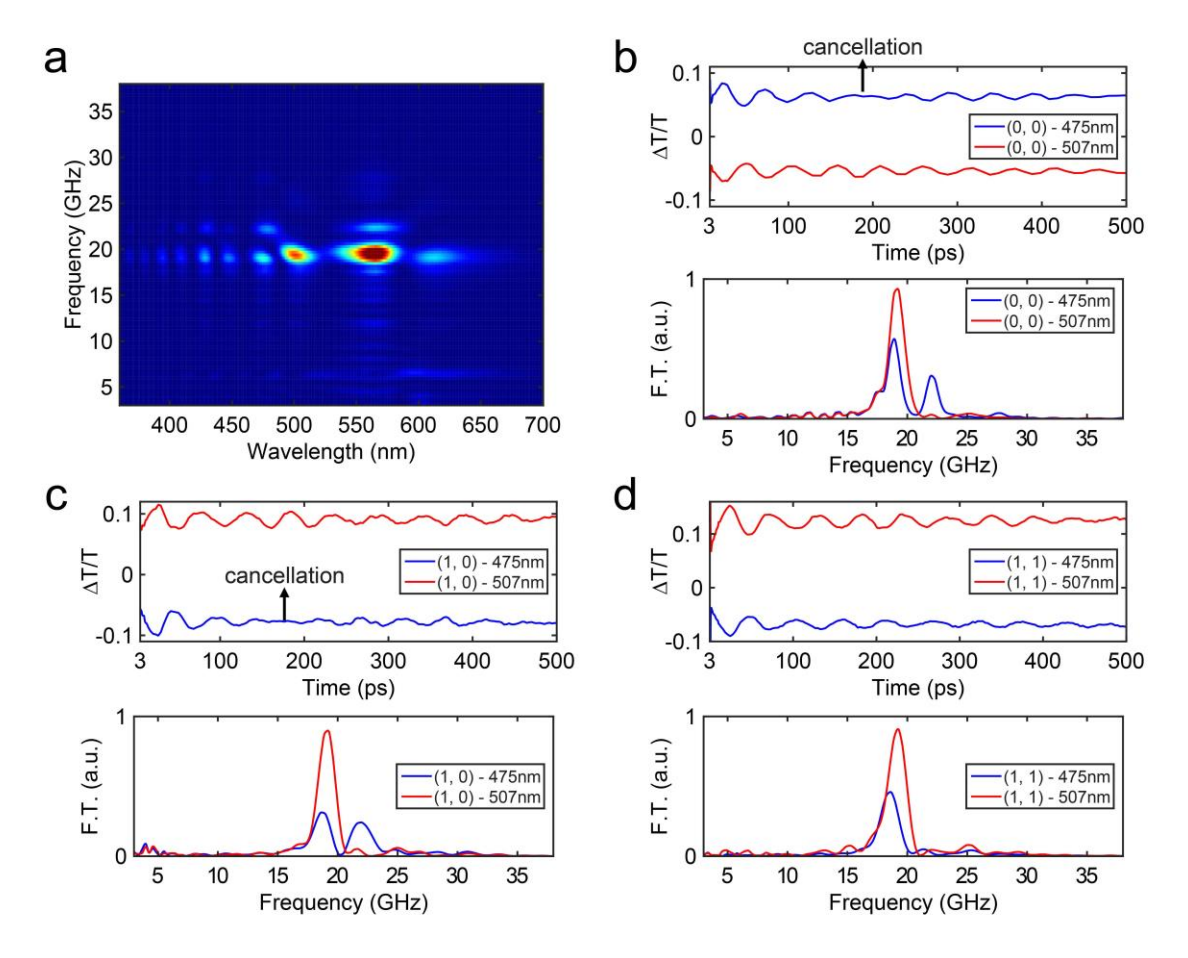


Fig. 3. Frequency signatures of the breathing modes. a, Fourier transform of the $\Delta T/T$ spectral map for the (0,0) mode shown in Fig. 2c. **b**, $\Delta T/T$ kinetics at 475 nm and 507 nm for the (0,0) mode and their corresponding Fourier transform. **c**, $\Delta T/T$ kinetics at 475 nm and 507 nm for the (1,0) mode and their corresponding Fourier transform. **d**, $\Delta T/T$ kinetics at 475 nm and 507 nm for the (1,1) mode and their corresponding Fourier transform.

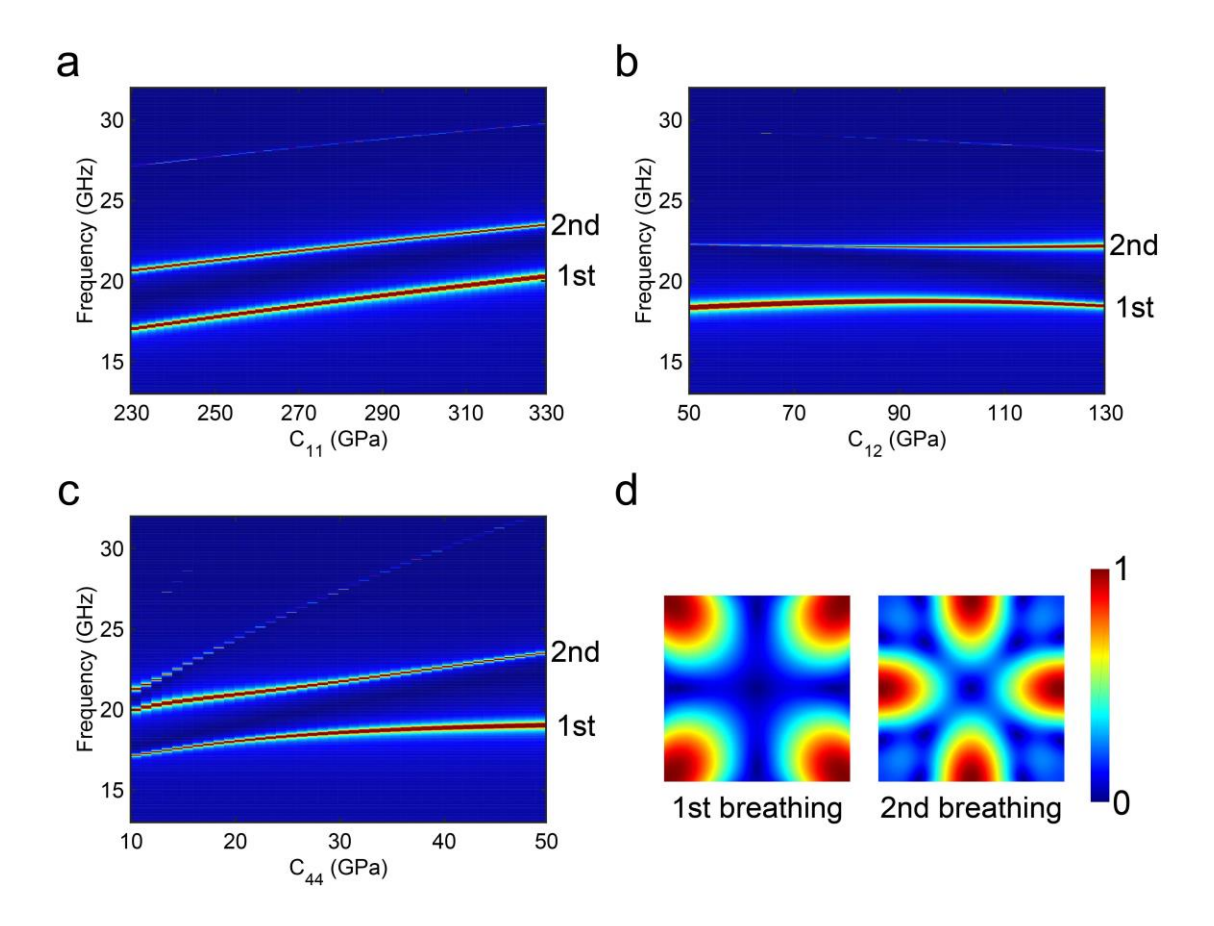


Fig. 4. Finite-element simulations of the breathing modes. a, **b**, **c**, 2D cross-section simulation predicted volumetric strain integrated over the entire nanorod cross-section plotted as a function of frequency (in the vertical axis) and C_{11} , C_{12} and C_{44} , respectively (in the horizontal axis). **d**, Displacement amplitudes for the 1st and 2nd breathing modes (linearly scaled into the range of 0 to 1). Edge length of the cross-section is 180 nm. The common elastic constants used in simulation are C_{11} =277.5 GPa, C_{12} = 107 GPa and C_{44} = 33.8 GPa.

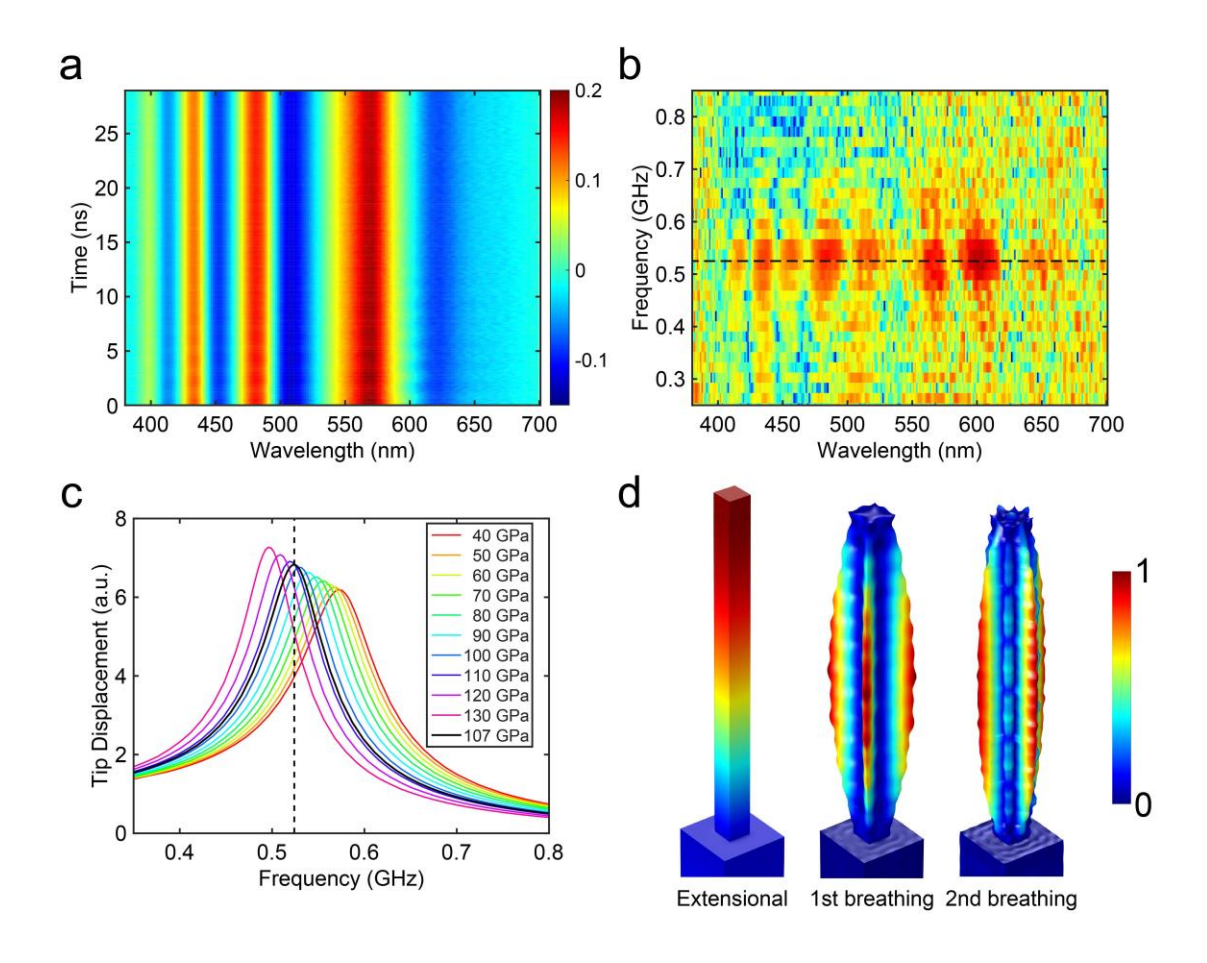


Fig. 5. Analysis of the extensional mode of the ITO-NRA. a, Δ T/T spectral map of the (0,0) mode for spectral range between 360 nm to 700 nm with delay time up to 28 ns. Pump fluence is 34.2 mJ/cm². b, Fourier transform of the Δ T/T spectral map shown in a. The dashed line shows the weighted average of the vibration frequency. c, Simulated displacement amplitude of the center of the nanorod top plane along the nanorod long axis for various C_{12} values plotted as a function of frequency. Nanorod height and edge length in the simulation are 2561 nm and 180 nm. C_{11} and C_{44} are 277.5 GPa and 33.8 GPa. d, Displacement amplitudes for the extensional mode and the two breathing modes. The displacement amplitude along the nanorod long axis is color-coded for the extensional mode; whereas total displacement amplitude is color-coded for the breathing modes. All displacement amplitudes are linearly scaled into the range of 0 to 1, and the deformation of the structure is linearly proportional to the corresponding displacement amplitudes.

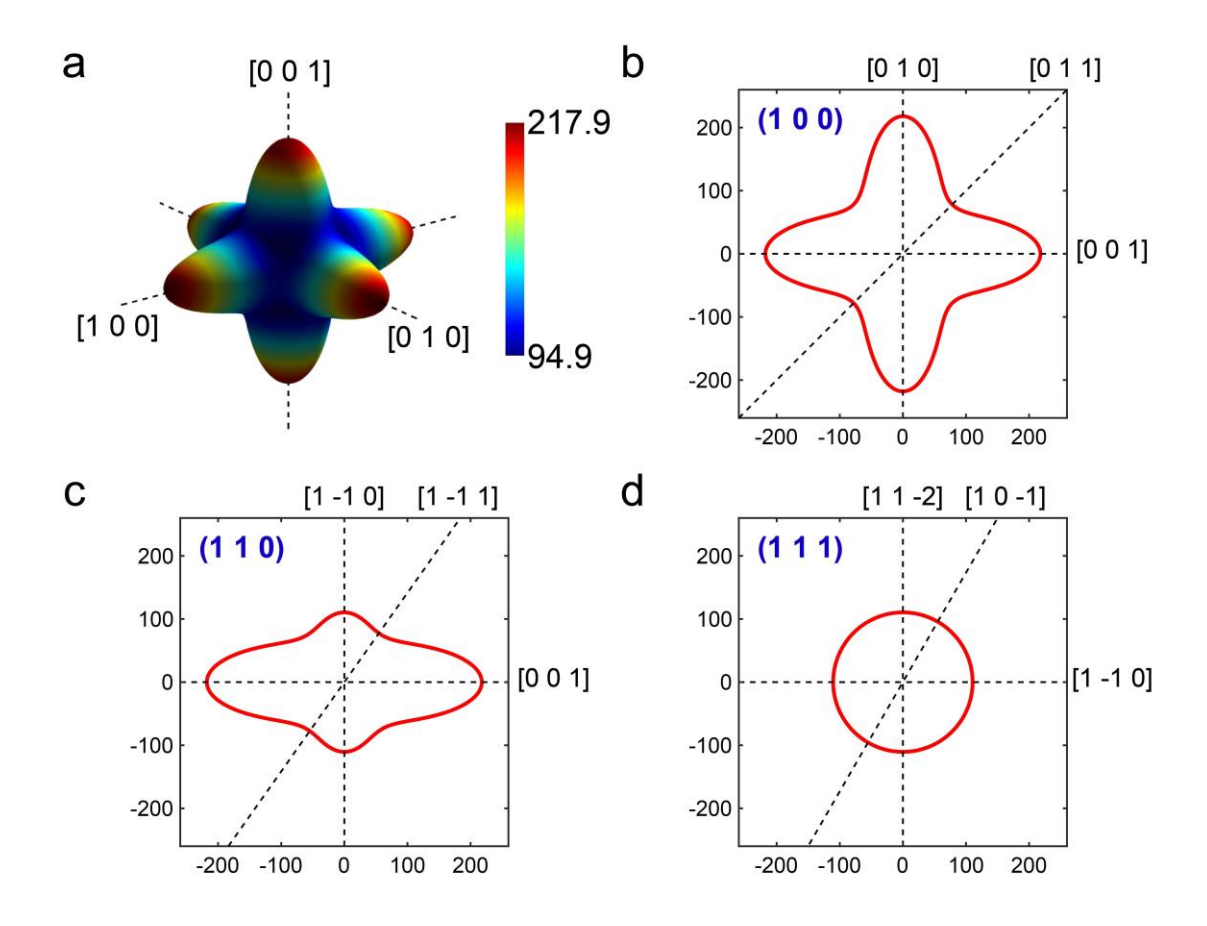


Fig. 6. Directional dependent Young's Modulus of ITO. a, Crystal-orientation dependent Young's modulus diagram for single-crystalline ITO. The distance from the origin to the surface is equal to the Young's modulus along that particular direction, and color-coded (unit for the color-bar is GPa). **b**, **c**, **d** Crystal orientation dependent Young's modulus for crystal directions in the (100), (110) and (111) planes, respectively. Certain low-index directions are shown by the dashed line.

Supplementary Material

Click here to access/download **Supplementary Material**acoustic_SI_20160121_references_in_main_text.docx